Applied Surface Science 314 (2014) 322–330

Contents lists available at ScienceDirect

Applied Surface Science

journal homepage: www.elsevier.com/locate/apsusc

Loss of implanted heavy elements during annealing of ultra-shallow ion-implanted silicon: The complete picture

T.K. Chan [a,*], S.Y. Koh [a], V. Fang [b], A. Markwitz [b,c], T. Osipowicz [a]

[a] Centre for Ion Beam Applications, Department of Physics, National University of Singapore, Singapore 117551, Singapore
[b] Department of Ion Beam Technologies, GNS Science, Gracefield 5010, New Zealand
[c] The MacDiarmid Institute for Advanced Materials and Nanotechnology, Kelburn, Wellington, New Zealand

ARTICLE INFO

Article history:
Received 18 March 2014
Received in revised form 9 May 2014
Accepted 5 June 2014
Available online 10 July 2014

Keywords:
Ion implantation
Ultra-shallow junctions
Dopant dose loss
Group IV alloys
High-resolution RBS
Crystal regrowth

ABSTRACT

From the observations of the annealing process of ultra-shallow Sn and Pb implanted Si, we propose the mechanism and the triggering conditions for the dopant dose loss effect commonly observed in heavy ion-implanted silicon. The results of high-resolution Rutherford backscattering spectrometry, high-resolution cross-sectional transmission electron microscopy and Monte Carlo simulations are presented. With these results, we construct a complete chain of events that leads to the loss of most of the implanted ions. First, the implanted atoms agglomerate into liquid melts during high temperature electron beam annealing, causing polycrystalline phase formation. Next, liquid phase movement takes place along grain boundaries, and the implanted atoms are forced out of the surface layer as the grain boundaries disappear during grain growth, leaving behind low concentrations of residual atoms. The specific conditions that trigger such a sequence of processes are identified.

1. Introduction

Ion implantation using ion beams is a well-established technique used in many materials systems, e.g. for the creation of novel materials and for dopant introduction in semiconductors at concentrations well above the maximum equilibrium solid solubility. Its advantage lies in its capability for precise tailoring of the concentration and depth profile of the implanted ions, with a strict control of the ion incident energy and fluence. In contrast to commonly used film deposition methods such as chemical vapor deposition (CVD) where the phase of the films (monocrystalline, polycrystalline or amorphous) is determined by the deposition conditions, a subsequent annealing process is required after ion implantation in order to induce crystal regrowth by solid phase epitaxy (SPE). This is important for dopant activation in silicon device manufacturing where implanted atoms (dopants) are required to occupy substitutional sites.

For heavy implanted ions such as In [1], Sn [2,3], Sb [4] and Pb [5,6] in silicon, progressive lattice reconstruction with SPE indeed occurs at implantation doses below a certain threshold dose. However, at implantation doses which exceeds the threshold, polycrystalline phase formation occurs instead of SPE and significant losses of the implanted atoms occur after the grain growth process to the monocrystalline phase. The threshold dose varies for different combinations of implanted atom and substrate elements. Such a dopant dose loss effect presents a serious problem for ultra-shallow junctions, where incomplete activation as well as the loss of implanted In [7] and Sb [8,9] after annealing occurs at high dopant concentrations. Indeed, a recent study of Sb implanted Si [9] revealed that the Sb loss exceeds 80% for an implantation fluence of $1 \times 10^{15}\ \mathrm{cm}^{-2}$. Such losses severely limit the usefulness of heavy-ion implantation as a method for creating ultra-shallow junction, heavy-dopant introduction, or band gap engineering of novel materials in Si photonics research. This has since led to research in co-implantations [10,11] in an effort to improve dopant retention during ion implantation. To date, there is no clear picture of what triggers the polycrystalline phase formation and how this is linked to the loss of the implanted ions. A clear understanding of the implanted atom loss process during annealing, as well as the conditions which trigger such a phenomenon, is important for the ongoing heavy-ion implantation research.

Apart from modeling the dopant dose loss effect, the use of Sn and Pb implantations in Si also illustrate the research in Group IV semiconductors, which has potential applications in photonic devices capable of monolithic integration with existing Si devices and platforms [12]. The recent demonstration of direct band gap

* Corresponding author.
E-mail addresses: tawkuei@gmail.com, phyctk@nus.edu.sg (T.K. Chan).

http://dx.doi.org/10.1016/j.apsusc.2014.06.030

luminescence in Ge for GeSn semiconductor alloys [13] has sparked intense research interest in such alloys. However, the relative scarcity and the high cost of Ge remains an obstacle to future industrial mass production. Nonetheless, the mechanism of the dopant dose loss effect described here is quite likely to also be applicable in heavy-ion implanted Ge.

Modern research now requires the investigation of thin films and junction depths with thicknesses of only several nanometers. Meaningful characterizations must therefore be performed using methods with high depth resolution. High-resolution Rutherford backscattering spectrometry (HRBS) [14] is capable of non-destructive and quantitative elemental profiling with sub-nanometer depth resolution for heavy elements. High-resolution cross-sectional transmission electron microscopy (XTEM) provides high-magnification imaging for identification of the crystalline phase.

In our previous work [15], results showed a progressive advance of the amorphous/crystalline interface in Sn implanted Si samples due to SPE at low implantation fluence. There was no movement of the implanted Sn atoms even at annealing temperatures far exceeding the melting point of Sn, and the implanted region remains amorphous throughout the annealing process. Such a SPE regrowth process is favorable for practical applications as the Sn atoms are retained and they occupy substitutional sites after SPE.

In this work, we present observations on the crystal regrowth process where a transformation to the polycrystalline phase has occurred instead of SPE during the annealing of Sn and Pb implanted Si samples at higher fluences. HRBS, high-resolution XTEM measurements as well as Monte Carlo simulations were performed to determine the characteristics of the grain growth process of the polycrystalline phase within a depth of 50 nm. From the entirety of these results, we construct a complete chain of events that leads to the loss of most of the implanted atoms and identify the conditions which trigger such a chain of processes. This series of phenomena may apply to all heavy-ion implanted samples with low implant element melting point, and is not just limited to Group IV alloys of Si.

2. Experimental

Samples were prepared at GNS Science, New Zealand [16]. Focused beams of heavy ions produced by a Penning sputter ion source from solid materials were scanned across the target surfaces. Identical n-type Si(1 0 0) substrates for all samples were first self-amorphized at room temperature with 25 keV Si^+ ions at a fluence of 5×10^{14} cm^{-2}. For Sn-implanted Si samples, 20 keV Sn^+ implantations were performed separately at fluences of 5×10^{15} and 1×10^{16} cm^{-2}. For cross-sectional TEM analysis, Sn implanted sample at 2×10^{15} cm^{-2} from our previous work is also included in the analysis. For Pb-implanted Si samples, 20 keV Pb^+ implantations were performed at a fluence of 2×10^{15} cm^{-2}. For simplicity, this paper shall refer to 2×10^{15}, 5×10^{15} and 1×10^{16} cm^{-2} as low, medium and high fluence, respectively. Each implanted sample undergo electron beam annealing at temperatures up to 800 °C at 500 s duration. During annealing, a focused 20 keV high current electron beam of 3–4 mA was raster scanned over the sample with temperature gradients of 5 °C s^{-1} during the heating and cooling phases of the annealing cycle. At peak temperature, an accuracy of ±1 °C was obtained using a computer controlled feedback system. Both ion implantation and electron beam annealing are carried out in high vacuum of $\sim 10^{-7}$ mbar.

HRBS measurements were performed at the Centre for Ion Beam Applications at the National University of Singapore [14]. A beam of 500 keV He^+ ions was generated by a 3 MV Singletron accelerator and was collimated to a divergence angle of <1 mrad. The beam was incident on each sample, which was mounted on a high precision 5-axis goniometer within a UHV scattering chamber of $<5 \times 10^{-9}$ mbar. Ions scattered at 65° were analyzed by a 90° double-focusing magnetic spectrometer and were collected by a 100-mm 1-D position sensitive resistive-strip focal plane detector. Our detection system has an energy resolution of ∼1 keV at 500 keV incident beam energy, which allows for sub-nanometer depth resolution for heavy elements. Aligned spectra were measured with the beam travelling along the ⟨111⟩ channeling axis of the Si substrate. High resolution XTEM imaging was performed on sample cross-sections, using a 200 keV JEOL2010F field emission machine.

3. Results: HRBS, XTEM and T-DYN

Fig. 1 shows the HRBS spectra of medium and high fluence samples of Sn implanted Si, respectively. The spectra for individual samples are shown in Figs. A.1, A.2 and A.3 in the Appendix. The as-implanted Sn profile display peak concentrations of 6.4 at% and 11.4 at%, respectively for medium and high fluences, as fitted by the SIMNRA simulation code [17]. Upon annealing, both sets of samples show Sn redistribution, with significant accumulation within a 5 nm depth at the surface. Such an effect is normally undetectable by conventional RBS using solid state surface barrier detectors, due to the lack of depth resolution. The aligned spectra of the Si signal also indicate that crystal regrowth has taken place to a larger extent with increasing annealing temperature accompanied by a corresponding decrease in the depth of Sn redistribution, indicating that SPE and polycrystalline phase formation are competing processes. Both sets of sample achieved the monocrystalline phase during annealing at 800 °C, accompanied by the loss of most of the Sn atoms. However, a broadly distributed, low level of residual Sn remains, situating at mean depths of ∼18 nm and ∼24 nm for medium and high dose samples, respectively.

Fig. 2 shows the high-resolution XTEM images of the Sn implanted Si samples. Fig. 2(a) shows that the low fluence Sn sample from our previous work [15] remains amorphous during annealing at 520 °C, and progressive SPE regrowth occurs. No Debye-Scherrer rings are detected for this sample under diffraction mode. Fig. 2(b) and (c) shows the polycrystalline phase formation for samples at medium and high fluences. A smaller average grain size is seen in the high fluence sample, indicating a lower grain growth rate for higher implantation fluence. The Debye-Scherrer rings are seen in diffraction mode, shown in the inset of Fig. 2(c), confirming the formation of the polycrystalline phase.

Fig. 3 shows the random and aligned HRBS spectra for the low fluence Pb implanted Si samples annealed between 400 and 800 °C. The as-implanted peak Pb concentration is 4.3 at%. At 400 °C anneal, there is yet no movement in Pb and the SPE a/c front is still at a depth of ∼38 nm. By 500 °C, however, most Pb atoms are lost, with the remaining non-crystalline Si signal being roughly half the height of the random level, indicating that the layer is no longer amorphous. By 800 °C, the crystal regrowth is complete, leaving behind residual Pb at two distinct mean depths of ∼25 nm and ∼15 nm. Note that for the 800 °C random spectrum, some slight ion channeling had still occurred, resulting in a lower random Si signal. Our results are in good agreement with previous conventional RBS studies of ion implanted Pb in Si [5,6].

Fig. 4 shows the high-resolution XTEM micrographs for the low fluence Pb implanted Si samples annealed at 400 °C and 600 °C. Results show dark spots distributed over a depth range of 15–21 nm from the surface for the 400 °C sample, which suggests the start of the polycrystalline phase formation. The magnified view in the inset of Fig. 4(a) shows that the spots appear to be small polycrystallites. It is not possible to identify the elemental identity of these crystallites, but we believe these are in fact Si crystallites which

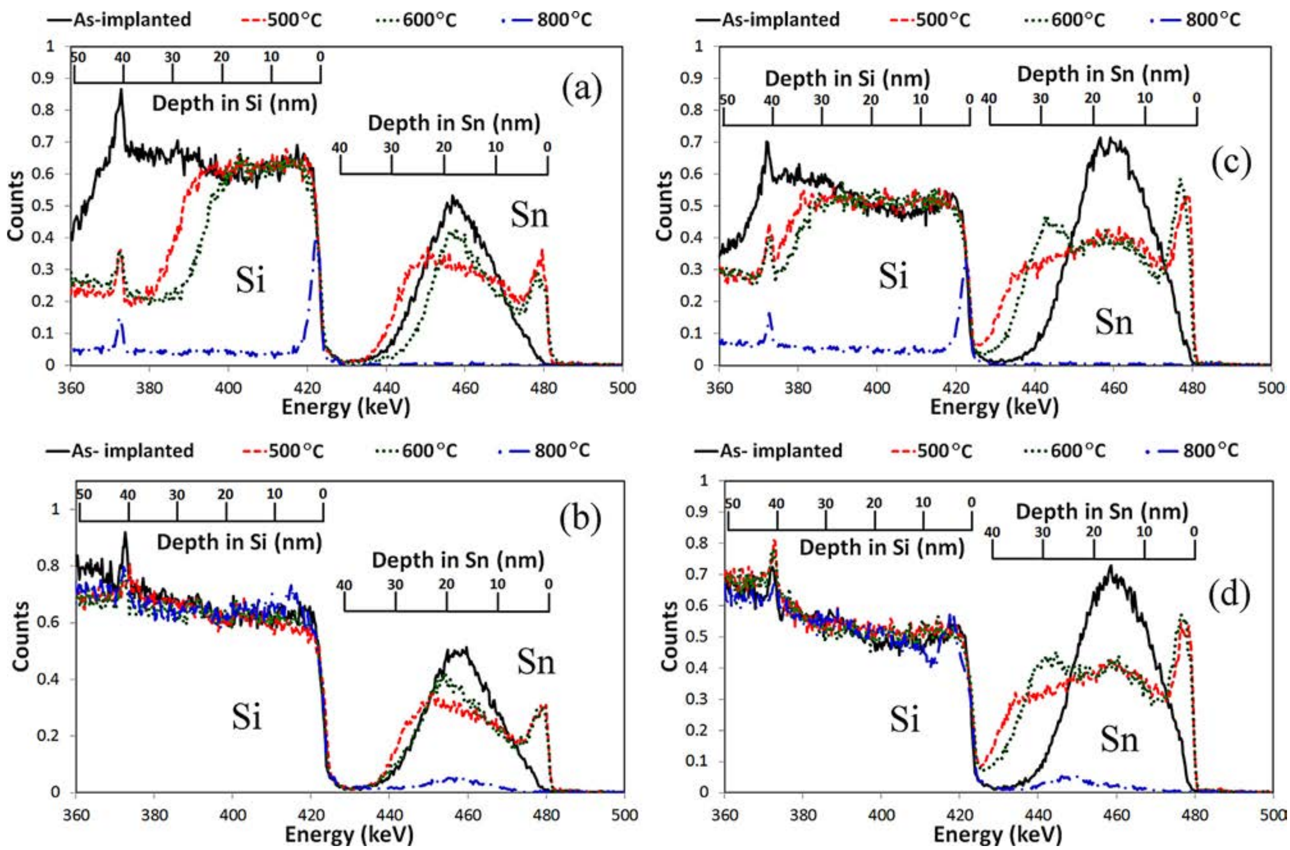

Fig. 1. HRBS spectra of Sn implanted spectra for (a) and (b) 5×10^{15} cm^{-2} fluence, (c) and (d) 1×10^{16} cm^{-2} fluence. (a) and (c) show the ⟨111⟩ aligned spectra while (b) and (d) show the random spectra.

we shall refer to as "polycrystallites". These polycrystallites are the result of the moving agglomerations of the implanted atoms in the liquid phase and eventually lead to the polycrystalline phase formation of the implanted layer. This process will be elaborated on in the next section. At this stage, the crystallite formation occurs with no significant movement in Pb, probably due to the low dissolution rate of Si into the melts at such a low annealing temperature (400 °C). The 600 °C sample displayed a polycrystalline layer of ~15 nm thickness, in good agreement with the HRBS results in Fig. 3. The layer structure is dominated by large twin defects, which accounts for the Si signal in the channeled alignment being about half the random height, as the ions are only partially channeled in the twin defect region.

Fig. 5 shows a Monte Carlo dynamic TRIM (T-DYN) [18] simulation for the ion-induced defect density for Sn and Pb implanted samples at various fluences. Such low energy heavy ions generate massive defect densities with highly non-uniform, sharply peaked depth profiles. Here, it is important to note that the peak defect densities for all samples are at 10–15 nm, preceding the peak concentrations at 15–20 nm of depth.

4. The complete picture

An amorphous-to-polycrystalline transformation in 100 keV Sn implanted Si samples was reported by Thornton et al. [2] for sufficiently high fluences. It was proposed that the mobile Sn-rich melts move about in the liquid phase within the initially amorphous environment during annealing, leaving behind trails of polycrystallites. There is, however, no mention of the subsequent grain growth process and how it leads to the loss of the implanted ions. Here, from all the results presented, we construct a complete picture of the entire process, from the initiation of Sn melt agglomeration to the completion of the grain growth.

The chain of events begins with the agglomeration of implanted ions into melts, which is initiated by a threshold implant concentration. Figs. 3 and 4 indicate that agglomeration occurred in a region corresponding to the peak concentration region (15–20 nm) and not at the peak defect region (10–15 nm). A region with a high concentration of implanted atoms results in an average close proximity of these atoms within an amorphous environment. Neighboring implanted atoms may then form implant-rich agglomerations, which are in the form of liquid melts due to the melting point of the implant element (in this case, Sn at 232 °C and Pb at 327.5 °C) being lower than the annealing temperature. The exact threshold concentration of implant that will trigger agglomeration is, however, different for different implant/substrate element combinations. In our case, the binary phase diagrams of Si–Sn [19] and Si–Pb [20] display almost horizontal solidus lines at temperatures near the melting points of Sn and Pb, respectively, while the liquidus temperatures are generally above 1000 °C for both. This means that within the melts, solid silicon coexists within a liquid Sn-rich or Pb-rich phase during annealing at 500 °C.

The next step along the chain is the melts becoming mobile. In Fig. 5, T-DYN simulations show that low energy heavy ions implantations invariably lead to a sharply peaked defect density profile which precedes the depth position of the concentration peak. This results in the melts existing in a region with a very large defect density gradient. Such a non-uniform environment induces a difference in dissolution and nucleation rate of Si within the melt, resulting in a Si concentration gradient which drives a movement of Si across the melt. The melts thus begin to move, leaving behind trails of Si polycrystallites, whose formation is facilitated by the preferential sites for Si crystal nucleation generated by the ion induced defects

Fig. 2. High-resolution XTEM micrographs of Sn implanted Si samples at (a) low fluence annealed at 520 °C, (b) medium fluence and (c) high fluence, both annealed at 500 °C. Inset in (c) shows Debye-Scherrer rings in diffraction mode. The implanted region remains amorphous during annealing for low fluence while polycrystalline phase forms for medium and high fluences. (c) Shows a smaller average grain size as compared to (b), indicating a retarded rate of grain growth for high fluence.

Fig. 3. HRBS (a) aligned and (b) random spectra for low fluence Pb implanted Si.

with the absence of a proper crystalline seed layer [21]. Fig. 1 shows significant re-distribution of Sn while Fig. 2 confirms the formation of the polycrystalline phase at 500–600 °C of anneal. The melt movement speed depends on the Si dissolution rate and hence the annealing temperature, but such a liquid phase movement is faster than the solid phase lattice reconstruction process of SPE. Upon the completion of these processes, a complete polycrystalline layer is formed, along with a polycrystalline–crystalline (p/c) interface with the Si substrate.

The melts now exist in a completely polycrystalline environment and are now free to diffuse along the grain boundaries, which are regions of high free energy within the polycrystalline environment. At the same time, grain growth of the polycrystallites occurs as the annealing process continues. The p/c interface acts as an impenetrable barrier to the melts while the surface native oxide appears to form only a temporary barrier to the melt movement. Hence, as grain growth proceeds, the liquid melts are "squeezed out" of the layer from the surface along with the disappearing grain boundaries, and are mostly lost from the samples upon complete grain growth into monocrystalline phase. Indeed, Figs. 1 and 3 show the loss of most of the implanted Sn and Pb atoms by 800 °C of anneal. The chain of events is now complete.

It is important to note that the melt movement occurs in two stages. The first stage is the movement of agglomerated melts during the initial formation of the polycrystalline phase, where there is mainly only redistribution within the implanted region and no drastic loss of the implant element. The second stage is the liquid phase movement along grain boundaries during grain growth, where disappearing grain boundaries causes the loss of implant atoms through the sample surface.

Furthermore, as the movement and loss of the implanted atoms are in liquid phase along grain boundaries, the mechanism of dose loss presented here should also hold for doping implants such as

with each defect profile gives the high/low (H/L) defect density interface at depth positions of ~19 nm and ~24 nm for medium and high fluence Sn samples and ~15 nm for the low fluence Pb sample, respectively. In Figs. 1 and 3, we see that the mean positions of the residual atoms at 800 °C anneal show good agreement with their respective H/L depth positions, indicating that some implanted atoms appear to be trapped at such H/L interfaces. The residual atoms appear to be substitutional for Sn with only one broad distribution (Fig. 1). For Pb, there are two narrow distributions of residual atoms, at ~15 nm (non-substitutional) and ~25 nm (substitutional), as shown in Fig. 3.

The exact mechanism of such a trapping phenomenon remains unclear at this stage; it could happen in the solid or liquid phase. Our results cannot account for the difference in the number of distributions and in the substitutionality between the Sn and Pb residual atoms. However, we postulate the following sequence of events for Pb. For trapping in the solid phase, the residual accumulation at 25 nm may be due to Pb atoms caught by the SPE process as the a/c front swept by, due to its narrower defect profile. Also, Fig. 4(b) shows a late stage of grain growth where the entire layer consists of large grains in twin formation, anchored to the crystalline substrate at the H/L interface (15 nm), forming inverted V-shaped enclosures near the interface. The shallower implant atoms may also be trapped in these enclosures during the elimination of the odd plane of the twin as the layer transforms into the proper crystalline state.

As for trapping in the liquid phase, the residual atoms may be the result of the cooling of the trapped melts remaining within the sample at H/L interfaces. However, the transfer of Si in and out of the melts is a non-equilibrium process in a background of highly non-uniform defect density, the composition of the melts may be constantly changing as the melts move within the region. Melts at different depth regions may therefore have different compositions when they cool. This effect may be compounded by the different rates at which grain boundaries disappear, due to non-uniform grain growth rate in the region. Retention of Pb has been studied for co-implantation with C [24], N [25] and other elements [26] in Si. However, the mechanisms may differ due to the presence of co-implant elements.

7. Conclusion

In conclusion, we have performed HRBS, high-resolution XTEM and Monte Carlo T-DYN simulations on Sn and Pb implanted Si samples in order to understand the characteristics of the polycrystalline formation as well as the subsequent grain growth processes. We present a complete picture of the complete sequence of events leading to full grain growth and the loss of most of the implanted atoms. In short, agglomeration of implanted atoms into melts is induced by a threshold local concentration during annealing. These mobile melts lead to the formation of a fully polycrystalline layer, after which they travel along grain boundaries. During grain growth, the melts are forced out of the layer due to disappearing grain boundaries, leaving behind low level residual atoms near H/L interfaces.

From a good understanding of these event sequences, further research in novel implantation conditions may lead to higher degrees of retention of implanted heavy ions in substitutional sites. The key may be to avoid the trigger which leads to polycrystalline formation, and to restrict the crystal regrowth process strictly to the solid phase (SPE), avoiding the formation of the liquid phase.

Appendix A.

See Fig. A.1, Fig. A.2, Fig. A.3.

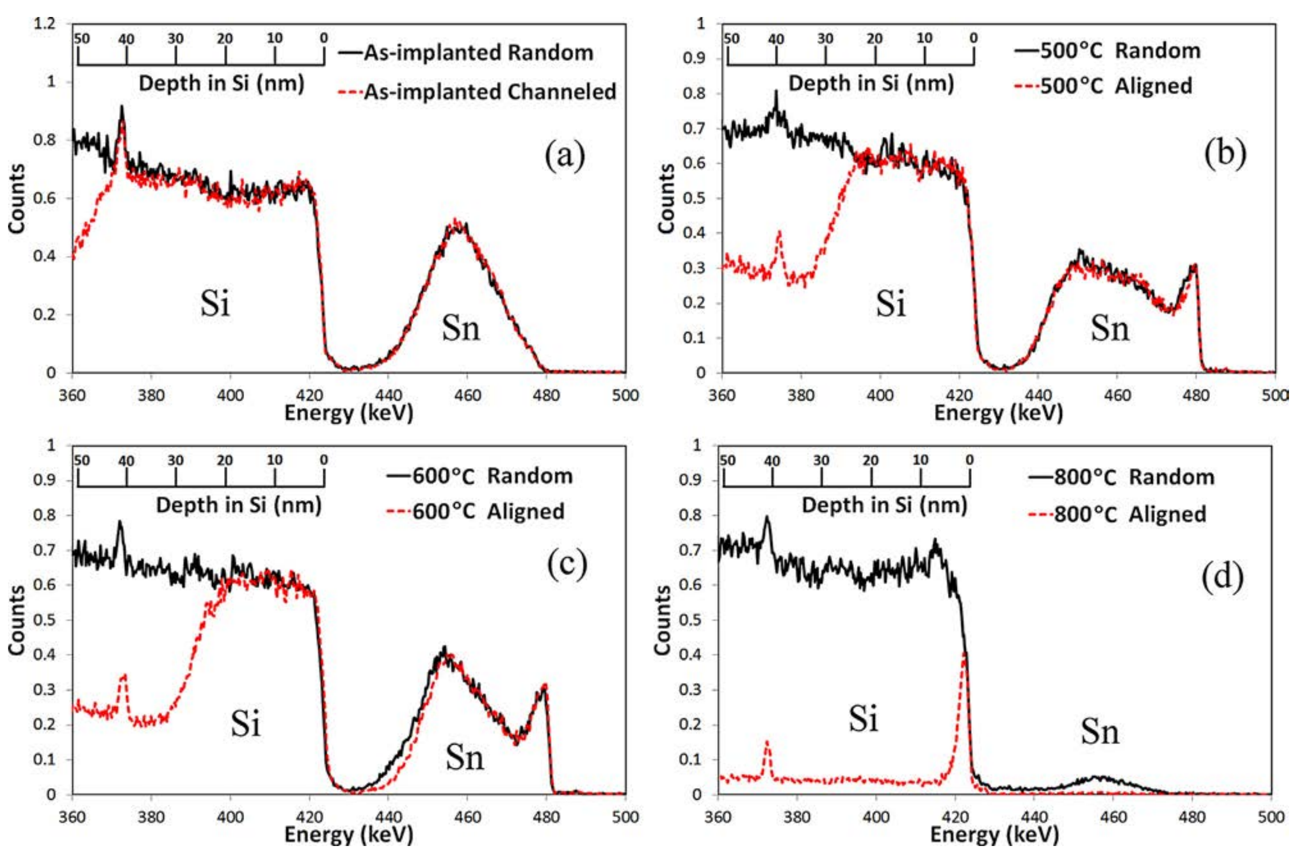

Fig. A.1. Individual HRBS spectra of medium fluence (5×10^{15} cm^{-2}) Sn samples for (a) as-implanted sample, (b) 500 °C, (c) 600 °C and (d) 800 °C annealed samples.

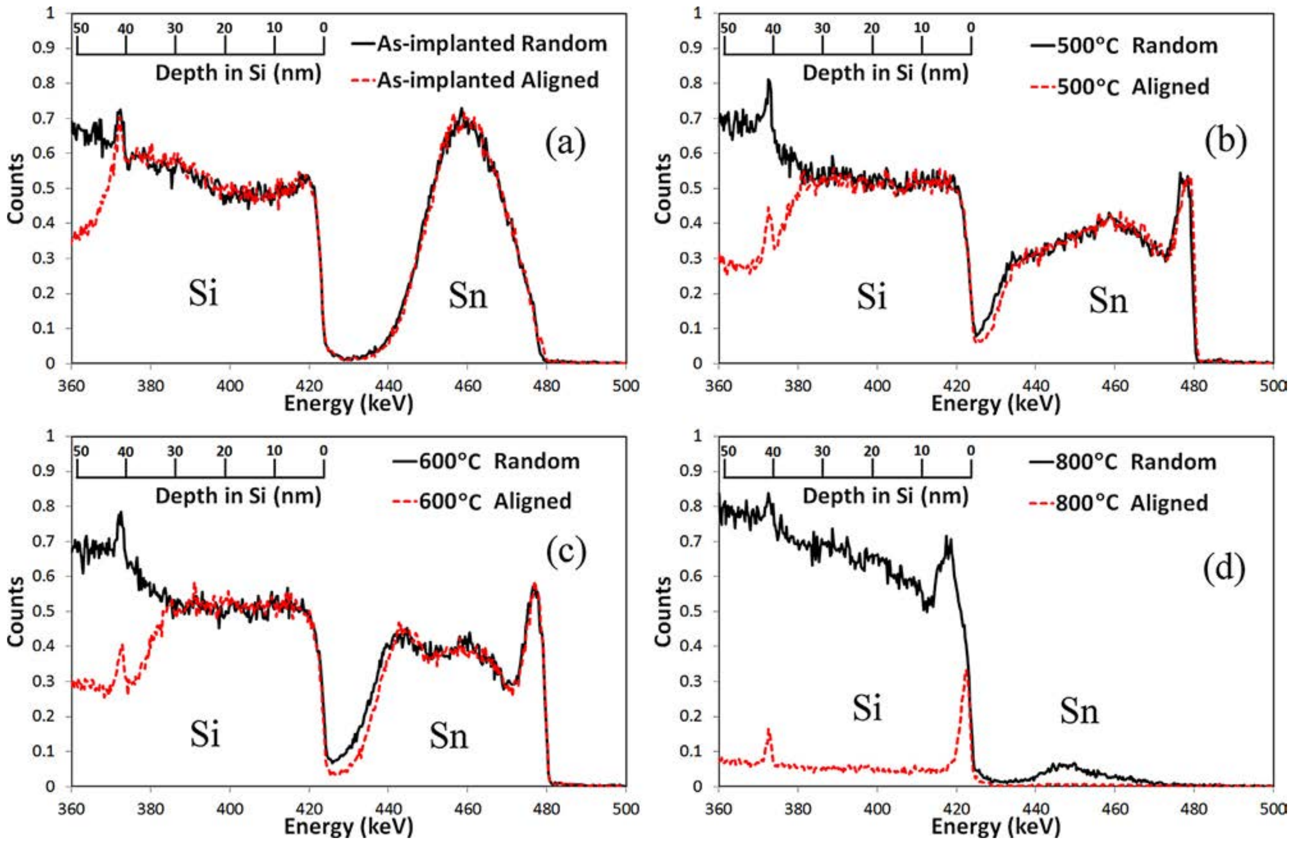

Fig. A.2. Individual HRBS spectra of high fluence (1×10^{16} cm^{-2}) Sn samples for (a) as-implanted sample, (b) 500 °C, (c) 600 °C and (d) 800 °C annealed samples.

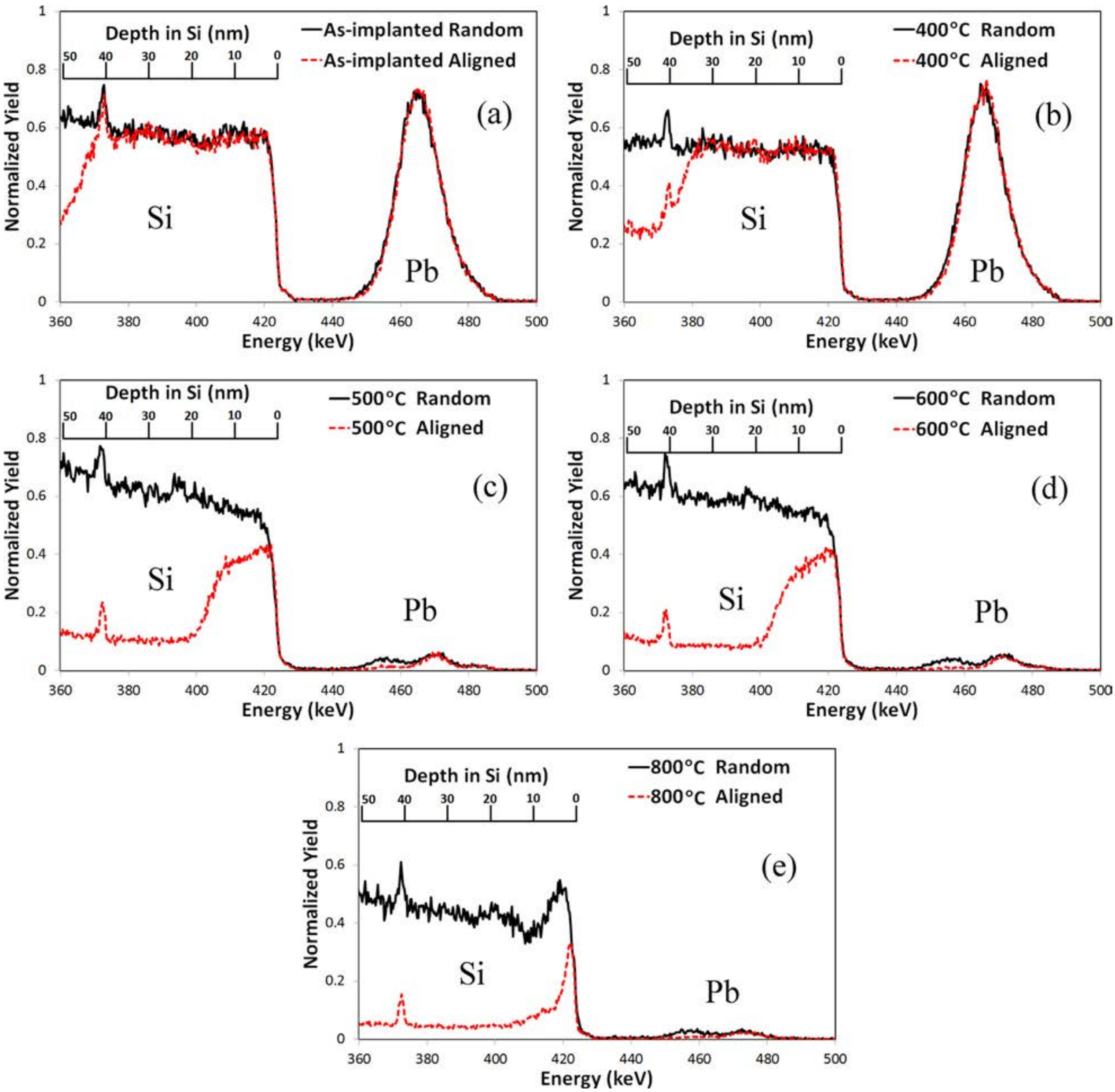

Fig. A.3. Individual HRBS spectra of low fluence (2×10^{15} cm^{-2}) Pb samples for (a) as-implanted sample, (b) 400 °C, (c) 500 °C, (d) 600 °C and (e) 800 °C annealed samples.

References

[1] E. Nygren, A.P. Pogany, K.T. Short, J.S. Williams, R.G. Elliman, J.M. Poate, Impurity-stimulated crystallization and diffusion in amorphous silicon, Appl. Phys. Lett. 52 (1988) 439–441.
[2] R.P. Thornton, R.G. Elliman, J.S. Williams, Amorphous-to-polycrystalline phase transformations in Sn-implanted silicon, J. Mater. Res. 5 (1990) 1003–1012.
[3] D. Klinger, J. Auleytner, D. Zymierska, B. Kozankiewicz, L. Nowicki, A. Stonert, Pulsed laser annealing of Sn-implanted Si single crystal, J. Appl. Phys. 95 (2004) 2331–2336.
[4] Y. Takamura, A.F. Marshall, A. Mehta, J. Arthur, P.B. Griffin, J.D. Plummer, J.R. Patel, Diffuse x-ray scattering and transmission electron microscopy study of defects in antimony-implanted silicon, J. Appl. Phys. 95 (2004) 3968–3976.
[5] A. Markwitz, H. Baumann, P. Davy, C. Beckert, J. Kennedy, Sub-surface retention of Pb atoms in silicon after low-energy ion implantation and electron beam annealing, Nucl. Instrum. Meth. B 266 (2008) 1553–1557.
[6] A. Markwitz, P. Davy, J. Kennedy, H. Baumann, Nanostructuring at the surface of low-energy lead-implanted silicon by electron beam annealing, Surf. Interface Anal. 40 (2008) 931–934.
[7] P. Chen, Z. An, M. Zhu, R.K.Y. Fu, P.K. Chu, N. Montgomery, S. Biswas, Implant damage and redistribution of indium in indium-implanted thin silicon-on-insulator, Mat. Sci. Eng. B 114–115 (2004) 251–254.
[8] R. Labbani, R. Halimi, T. Laoui, A. Vantomme, B. Pipeleers, G. Roebben, Characterization of Si(111) crystals implanted with Sb^+ ions and annealed by rapid thermal processing, Mat. Sci. Eng. B 102 (2003) 390–397.
[9] M.N. Mesli, B. Benbahi, H. Bouafia, M. Belmekki, B. Abidri, S. Hiadsi, The effect of dopant dose loss during annealing on heavily doped surface layers obtained by recoil implantation of antimony in silicon, Surf. Rev. Lett. 20 (2013) 1350038.
[10] S. Gennaro, M. Barozzi, M. Bersani, B.J. Sealy, R. Gwilliam, Diffusion of indium implanted in silicon: the effect of the pre-amorphisation treatment and of the presence of carbon, Nucl. Instrum. Meth. B 237 (2005) 88–92.
[11] M. Rehana, S. Ahmed, E.U. Khan, Formation of co-implanted silicon ultra-shallow junctions for low thermal budget applications, Chin. Phys. Lett. 30 (2013) 016101.
[12] J. Kouvetakis, A.V.G. Chizmeshya, New classes of Si-based photonic materials and device architectures via designer molecular routes, J. Mater. Chem. 17 (2007) 1649–1655.
[13] R. Roucka, J. Mathews, R.T. Beeler, J. Tolle, J. Kouvetakis, J. Menendez, Direct gap electroluminescence from Si/GeSn p-i-n heterostructure diodes, Appl. Phys. Lett. 98 (2011) 061109.
[14] T. Osipowicz, H.L. Seng, T.K. Chan, B. Ho, The CIBA high resolution RBS facility, Nucl. Instrum. Meth. B 249 (2006) 915–917.
[15] T.K. Chan, F. Fang, A. Markwitz, T. Osipowicz, Solid phase epitaxy of ultra-shallow Sn implanted Si observed using high-resolution Rutherford backscattering spectrometry, Appl. Phys. Lett. 101 (2012) 081602.
[16] A. Markwitz, D.A. Carder, T. Hopf, J. Kennedy, T.K. Chan, A. Mücklich, T. Osipowicz, Formation of nanoclusters with varying Pb/Se concentration and distribution after sequential Pb^+ and Se^+ ion implantation into SiO_2, Nucl. Instrum. Meth. B 273 (2012) 199–202.
[17] M. Mayer, SIMNRA, a simulation program for the analysis of NRA, RBS and ERDA, AIP Conf. Proc. 475 (1999) 541–544.
[18] J.P. Biersack, S. Berg, C. Nender, T-DYN Monte Carlo simulations applied to ion assisted thin film processes, Nucl. Instrum. Meth. B 59–60 (1991) 21–27, Part 1.
[19] Si-Sn Binary Phase Diagram, in FactSage Database, Centre for Research in Computational Thermochemistry (CRCT), Ecole Polytechnique de Montreal, URL. http://www.crct.polymtl.ca/fact/phase_diagram.php?file=Si-Sn.jpg&dir=SGTE
[20] Si-Pb Binary Phase Diagram, in FactSage Database, Centre for Research in Computational Thermochemistry (CRCT), Ecole Polytechnique de Montreal, URL. http://www.crct.polymtl.ca/fact/phase_diagram.php?file=Pb-Si.jpg&dir=SGTE
[21] C. Spinella, S. Lombardo, F. Priolo, Crystal grain nucleation in amorphous silicon, J. Appl. Phys. 84 (1998) 5383–5414.
[22] A.Y. Azarov, A. Hallén, B.G. Svensson, A.Y. Kuznetsov, Annealing of ion implanted CdZnO, J. Phys. D 45 (2012) 235304.
[23] E. Friedland, N.G. van der Berg, T.T. Hlatshwayo, R.J. Kuhudzai, J.B. Malherbe, E. Wendler, W. Wesch, Diffusion behavior of cesium in silicon carbide at $T > 1000\,^{\circ}C$, Nucl. Instrum. Meth. B 286 (2012) 102–107.
[24] A. Markwitz, H. Baumann, P. Davy, P.B. Johnson, Diffusion of Pb in carbon ion-implanted silicon: discovery of a new crystalline phase after electron beam annealing, Vacuum 82 (2008) 1306–1311.
[25] A. Markwitz, F. Fang, P.B. Johnson, Dual N/Pb ion-implanted Si: temperature dependence of the novel shift of the Pb peak under electron beam annealing, Appl. Surf. Sci. 257 (2011) 4856–4862.
[26] A. Markwitz, F. Fang, H. Baumann, P.B. Johnson, Diffusion of Pb in (100) Si under electron beam annealing following dual ion implantations of Pb/Ne, Pb/O and Pb/N, Vacuum 84 (2010) 1103–1110.